

A Robust Evolutionary Particle Filter Technique for Integrated Navigation in Urban Environments via GNSS and 5G Signals

Yuan Zhang^{ID}, Graduate Student Member, IEEE, Rui Wang^{ID}, Senior Member, IEEE,
and Zhe Xing^{ID}, Member, IEEE

Abstract—This article focuses on integrated navigation systems using a combination of Global Navigation Satellite Systems (GNSS) and fifth-generation (5G) technology in urban environments. To address the challenge of accurately estimating the mobile terminal state in multipath environments, a robust evolutionary particle filter (REPF) technique is proposed. First, this article presents a modified clock compensation two-way pseudorange scheme that significantly improves pseudorange accuracy in nonideal line-of-sight/nonline-of-sight (LOS/NLOS) pseudorange environments. Then, this article derives the posterior belief conditioned on the obtained pseudorange measurements and velocity data from GNSS. Utilizing the aforementioned posterior distribution, we introduce a robust particle filter (RPF) algorithm to gauge both the sight state and localization in environments with multipath effects. To address the issue of particle degradation in the RPF algorithm, this article introduces a new evolutionary algorithm based on genetic theory to enhance the diversity of particle filtering. The proposed REPF technique is assessed in 5G ultradense networks, and simulation results demonstrate its achievement of accuracy in positioning and tracking at the meter level for moving targets in both LOS and NLOS environments.

Index Terms—Evolutionary algorithm, fifth generation (5G), Global Navigation Satellite Systems (GNSS) velocity, integrated navigation, nonline-of-sight (NLOS), robust evolutionary particle filter (REPF), ultradense networks.

Manuscript received 14 April 2023; revised 21 August 2023 and 2 December 2023; accepted 5 January 2024. Date of publication 25 January 2024; date of current version 4 April 2024. This work was supported in part by the National Natural Science Foundation of China under Grant 62271352, in part by the Shanghai Science and Technology Innovation Action Plan under Grant 21220713100, and in part by the Natural Science Foundation of Shanghai under Grant 22ZR1465100. Paper no. TII-23-1309. An earlier version of this article was presented in part at the 2023 IEEE International Conference on Communications (ICC) [DOI: 10.1109/ICC45041.2023.10279482]. (Corresponding author: Rui Wang.)

Yuan Zhang and Rui Wang are with the College of Electronics and Information Engineering, Tongji University, Shanghai 201804, China (e-mail: yuanzhang@tongji.edu.cn; ruiwang@tongji.edu.cn).

Zhe Xing is with the School of Information Science and Technology, North China University of Technology, Beijing 100144, China (e-mail: zxing@ncut.edu.cn).

Color versions of one or more figures in this article are available at <https://doi.org/10.1109/TII.2024.3353849>.

Digital Object Identifier 10.1109/TII.2024.3353849

NOMENCLATURE

Notation	Description
e_B or e_M	Deviations including the MT and BS_i from the nominal frequency.
s^i	i th element of vector s .
$\log(\cdot)$	Natural logarithm.
I_m	Identity matrix of size $m \times m$.
$\mathcal{N}(\mu, \sigma^2)$	Gaussian distribution with mean μ and variance σ^2 .

I. INTRODUCTION

IFTH-GENERATION (5G) communication networks demand precise user position and mobile terminal (MT) knowledge to enhance spatial services, such as pedestrian navigation [1], [2], Internet-of-Things support [3], and autopilot [4], [5]. Furthermore, 5G communication networks are projected to facilitate highly accurate MT positioning, particularly in line-of-sight/nonline-of-sight (LOS/NLOS) environments [6]. Current positioning methods, including Bluetooth, Wi-Fi, and Global Navigation Satellite System (GNSS) [7], provide positioning accuracy within a few meters. However, future real-time positioning services of 5G wireless communication aim for an accuracy of 1 m or even below [8].

Estimating MT's real-time location with high precision in 5G ultradense networks is emerging as an encouraging research endeavor. Koivisto et al. [9] introduced an integrated positioning and clock synchronization method. Wen et al. [10] presented an innovative tensor-based approach, thus enabling positioning and mapping using solely scattered multipath. Kim et al. [11] suggested a fresh technique for cooperative vehicle localization and environment mapping, integrating a multiple-model density filter and a map fusion procedure. Kanhere and Rappaport [12] elucidated the achievement of centimeter-level localization accuracy, especially employing map-based methodologies. Yin et al. [13] introduced an integrated GNSS methodology and device-to-device measurements in the 5G simulation environment.

Accurate cellular positioning in urban settings poses a significant challenge, primarily due to the prevalence of NLOS propagation within ultradense 5G networks. NLOS occurs as a result of the reflection and bending of radio signals, introducing a positive bias compared to LOS conditions and consequently compromising positioning accuracy. Moreover, NLOS propagation is a recurring obstacle across various communication

systems, including ultrawideband (UWB), fourth-generation (4G), and 5G. Given the complexities of urban landscapes, NLOS propagation is particularly probable in 5G systems, presenting substantial obstacles in achieving precise positioning. This challenge is especially relevant in areas such as autonomous ground vehicles (AGV) and pedestrian navigation. Gazzah and Najjar [14] proposed enhanced cooperative group localization with the identification of base stations (BSs) under LOS/NLOS propagation in 5G environment. Lin and Akyildiz [15] introduced BS formation for addressing NLOS issues in 5G communication networks. Wang et al. [16] devised an integrated localization algorithm for hybrid LOS/NLOS environments. The detrimental effects of NLOS were mitigated by exploiting the geometric relationship inherent in range biases. Specifically, the impact of NLOS signal propagation cannot be disregarded, i.e., MT in ultradense 5G networks not only acquires pseudorange information from LOS, but may also obtain pseudorange information from NLOS.

Expanding upon the foundations of 5G high-precision positioning and LOS/NLOS environments, we develop key facilitating technologies for integrated GNSS/5G positioning in 5G ultradense networks, where a resilient evolutionary particle filter (PF) technique is proposed. In comparison to our prior conference paper [17], we have further progressed the development of an innovative two-way pseudorange method to achieve accurate positioning. Our method involves the use of modified clock compensation two-way pseudorange (MCC-TWR). In addition, we introduce a new evolutionary algorithm based on genetic theory, which aims to enhance the diversity of particle filtering. Furthermore, we have carried out a thorough assessment of the computational complexity of this algorithm. Besides, we consider vital factors, such as path loss (PL), signal-to-noise ratio (SNR), and signal-to-interference plus noise ratio (SINR), especially regarding measurement noise variance in the context of 5G ultradense networks.

Specifically, the distinctiveness and technical contributions of this article are as follows.

- 1) We develop a novel two-way pseudorange method for accurate positioning by using MCC-TWR. The proposed method further reduces the impact of clock drift on time of flight (TOF) compared with previous methods.
- 2) We derive the posterior belief conditioned on the obtained pseudorange measurements and velocity data from GNSS. Taking into account the obtained posterior distribution, we propose a robust particle filter (RPF) algorithm in the LOS/NLOS scenario. This algorithm aims to estimate the sight state and position of the MT.
- 3) In order to mitigate particle degradation, we propose a new evolutionary algorithm based on genetic theory to enhance the diversity of particle filtering. We further evaluate the computational complexity of the proposed algorithm.
- 4) We conduct a comparison between our proposed evolutionary algorithm and the general PF. Furthermore, we extend the comparison to include the interacting multiple model-extended Kalman filter, evaluating its performance against our proposed REPF algorithm in the LOS/NLOS environments.

- 5) We evaluate the effectiveness of the introduced REPF technique in 5G ultradense networks. The comparison results show its capability to achieve meter-level accuracy in positioning and tracking for mobile targets in both LOS and NLOS environments.

The rest of this article is organized as follows. Section II gives the related work. Section III presents MCC-TWR in 5G ultradense networks. In Section IV, we present a GNSS/5G integrated navigation method that relies on an REPF technique. Section V assesses the performance of the proposed methodology through simulation. Finally, Section VI concludes this article.

In this article, the vector and the matrix are indicated by the bold lowercase and bold uppercase, respectively. The main notations used in this paper are summarized in the Nomenclature.

II. RELATED WORK

GNSS [7], [18], [19] encounter challenges when contending with multipath (also known as NLOS) effects. Multipath refers to the phenomenon where GNSS signals reach the receiver through multiple paths, leading to signal reflections, refractions, and diffractions. This can introduce inaccuracies in position estimation and degrade the overall performance of GNSS receivers. To tackle this issue, several techniques have been proposed for GNSS multipath. Lesouple et al. [20] formulated the GNSS positioning challenge as the resolution of an overdetermined system. This system involves variables, such as the receiver's spatial coordinates and velocity, clock offset, and drift, as well as potential biases impacting GNSS measurements. In [21], a unique multipath mitigation technique is suggested for general multipath situations. The proposed method is designed to address challenges arising from diverse multipath conditions. Hsu et al. [22] proposed the implementation of a vector delay lock loop with an adaptive extended Kalman filter. This approach replaces the traditional individual code-tracking loops and navigation filter while still maintaining the conventional carrier frequency tracking. Despite the ongoing emergence of various new research approaches to address the multipath problem in urban environments for GNSS, meeting the high-precision navigation requirements for scenarios, such as autonomous driving, remains challenging.

The integration of GNSS and 5G networks has garnered considerable attention from the research community due to the potential benefits it offers for positioning and location-based services. This integration can provide enhanced accuracy, reliability, and availability of positioning services, particularly in urban areas and indoor scenarios where GNSS signals may be attenuated or obstructed. Various research studies have explored the use of integrated GNSS and 5G positioning systems, particularly in the field of autonomous driving. These systems leverage satellite signals from GNSS in conjunction with signals from 5G networks to provide highly precise positioning and location data to self-driving vehicles. One strategy developed in [23] for navigation in GNSS-challenged environments involves utilizing signals of opportunity in a closed-loop map-matching manner. The proposed map-matching algorithm demonstrated a significant reduction in the root-mean-square error (RMSE) of position estimation, decreasing it by 74.88%, 58.15%, and 46.18% in three different environments, respectively, compared with an

exclusive long-term evolution (LTE)-only navigation solution. In [24], an optimal path planning generation approach based on the Dijkstra algorithm is developed for AGV. The method optimizes the AGV path while minimizing the path length and position mean square error, while ensuring that the position estimation uncertainty and bias due to multipath do not exceed the desired thresholds.

Recent studies on 5G networks have not fully exploited the abundance of information available from the system, such as time of arrival (TOA) and the potential influence of multipath propagation. To tackle this issue, Shamaei and Kassas [25] presented a comprehensive analysis of the 5G reference signals that could be utilized for navigation. They also proposed a software-defined receiver that could extract navigation observables from cellular 5G signals. The authors analyzed the statistics of code phase errors in both multipath-free and multipath environments. In another investigation, Chen et al. [26] sequentially conducted multipath acquisition and delay tracking to estimate the TOA of received signals. However, their approach to estimating the position of the user equipment solely relied on a weighted nonlinear least squares estimator, without considering the effects of multipath. It is crucial to take into consideration the effects of multipath or NLOS when estimating position, as multipath can introduce substantial errors in position estimation. Therefore, future research should strive to develop resilient algorithms that accommodate the impacts of multipath propagation in 5G-based navigation systems.

III. MCC-TWR IN 5G ULTRADENSE NETWORKS

Range measurements are utilized for precise localization, relying on the received signal strength or TOF from BS to MT. As indicated in Fig. 1(a), two-way pseudorange (TWR) enables BS-MT-based pseudorange to conduct TOF measurements without clock synchronization. Unfortunately, clock drift in the time reference system of devices inevitably impacts the estimated TOF between MT and BS. To mitigate the error caused by clock drift, a symmetric doubled-sided two-way pseudorange (SDS-TWR) scheme was proposed [27]. With the growing demand for high-precision positioning and minimal delay, further improvements in the performance of the current SDS-TWR pseudorange method are still required.

Let $\{\text{BS}_i\}_{i=1}^{\mathcal{M}}$ denote the set of BSs in 5G ultradense networks, where \mathcal{M} represents the total number of BSs. In this article, we focus on pseudorange, i.e., how to obtain the TOF between MT and BS_i . The core of the TWR is depicted in Fig. 1(a). To reduce the time errors caused by the clock drifts of the MT and BS_i , the main process of the proposed MCC-TWR is illustrated in Fig. 1(b). $t_t^{\text{MT},j}$ and $t_r^{\text{MT},j}$ denote the signal transmitting time and the signal receiving time in the j th round trip at MT. Similarly, $t_t^{\text{BS}_i,j}$ and $t_r^{\text{BS}_i,j}$ denote the signal transmitting time and the signal receiving time in the j th round trip at the i th BS. $T_{rt}^{\text{BS}_i,j}$ is the processing delay from the signal receiving time to the signal transmitting time in the j th round trip at the i th BS, where $j = 1, 2$, and $T_{rt}^{\text{MT},1}$ is the interval delay from the signal receiving time in the first round trip to the signal transmitting time in the second round trip at MT. $T_{tof}^{\text{BS}_i,j}$ is the propagation delay in the j th round trip at the i th BS, and $T_{tof}^{\text{MT},j}$ is the propagation delay in the j th round trip at MT, where $j = 1, 2$. The clocks of devices, including MT and BS_i , are assumed to be independent and

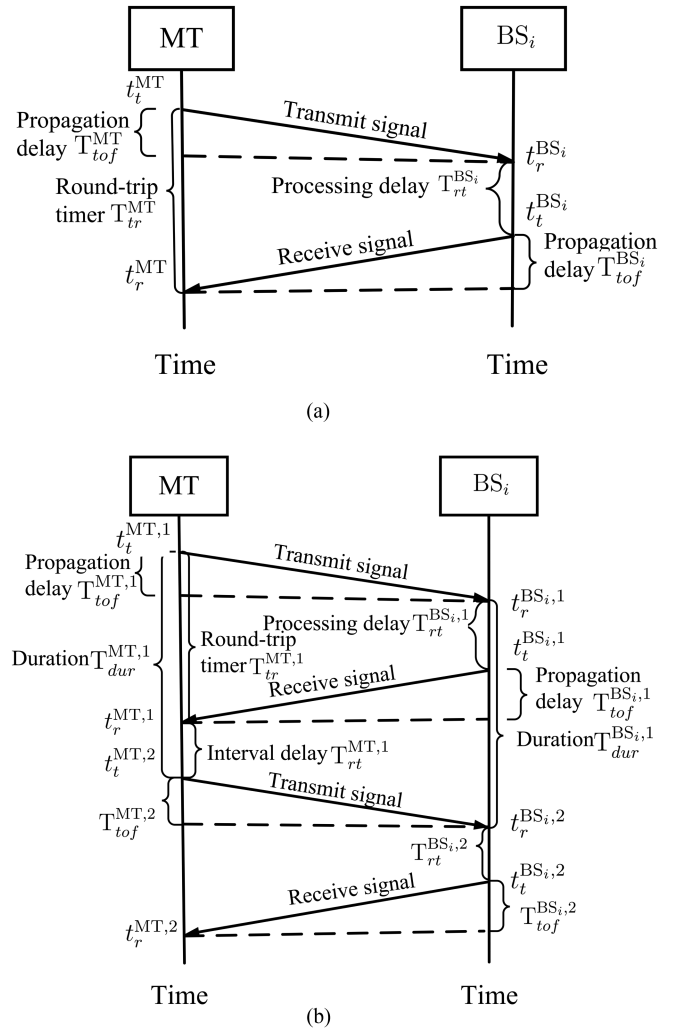


Fig. 1. Standard TWR and proposed MCC-TWR protocols. (a) Process of TWR scheme. (b) Process of proposed MCC-TWR scheme.

unsynchronized, and TOFs between the two devices are denoted as T_{tof}^{MT} at MT and $T_{tof}^{\text{BS}_i}$ at the i th BS, respectively. To facilitate analysis, $T_{tof}^{\text{MT}} = T_{tof}^{\text{BS}_i}$ is assumed for scenario Fig. 1(a).

Consider the ideal time reference system, as shown in Fig. 1(a)

$$T_{tr}^{\text{MT}} = T_{tof}^{\text{MT}} + T_{tof}^{\text{BS}_i} + T_{rt}^{\text{BS}_i} \quad (1)$$

where T_{tr}^{MT} and $T_{rt}^{\text{BS}_i}$ represent ideal measurements, respectively. Due to the imperfect effect caused by the clock drift in the time reference, we have

$$\hat{T}_{tr}^{\text{MT}} = (1 + e_M)T_{tr}^{\text{MT}}, \hat{T}_{rt}^{\text{BS}_i} = (1 + e_B)T_{rt}^{\text{BS}_i} \quad (2)$$

where \hat{T}_{tr}^{MT} is true measurement of round-trip timer from the signal transmitting time to the signal receiving time at MT, and $\hat{T}_{rt}^{\text{BS}_i}$ is true measurement of round-trip timer from the signal receiving time to the signal transmitting time at the i th BS, respectively. e_M and e_B are the deviations, including the MT and BS_i , from the nominal frequency, and are typically expressed in parts per million (ppm).

Considering $T_{tof}^{\text{MT}} = T_{tof}^{\text{BS}_i}$, the following derivation will take T_{tof}^{MT} in MT as the main consideration instead of $T_{tof}^{\text{BS}_i}$. Using the

time relationship in (1), we rewrite the estimated TOF given by

$$\hat{T}_{\text{tow}}^{\text{MT}, \text{TWR}} = (\hat{T}_{\text{tr}}^{\text{MT}} - \hat{T}_{\text{rt}}^{\text{BS}_i})/2 \quad (3)$$

and the estimated error of TWR is

$$\begin{aligned} \text{Error}_{\text{TWR}} &= \hat{T}_{\text{tow}}^{\text{MT}} - T_{\text{tow}}^{\text{MT}} \\ &= (\hat{T}_{\text{tr}}^{\text{MT}} - \hat{T}_{\text{rt}}^{\text{BS}_i})/2 - (T_{\text{tr}}^{\text{MT}} - T_{\text{rt}}^{\text{BS}_i})/2 \\ &= \frac{e_M T_{\text{tr}}^{\text{MT}} - e_B T_{\text{rt}}^{\text{BS}_i}}{2} \\ &= \frac{e_M (2T_{\text{tow}}^{\text{MT}} + T_{\text{rt}}^{\text{BS}_i}) - e_B T_{\text{rt}}^{\text{BS}_i}}{2} \\ &= e_M T_{\text{tow}}^{\text{MT}} + (e_M - e_B) T_{\text{rt}}^{\text{BS}_i}/2. \end{aligned} \quad (4)$$

Given that the processing delay $T_{\text{rt}}^{\text{BS}_i}$ or round-trip timer $T_{\text{tr}}^{\text{MT}}$ ($T_{\text{rt}}^{\text{BS}_i} < T_{\text{tr}}^{\text{MT}}$) is as low as 1 ms, the worst-case value of $e_M - e_B$ in IEEE 802.15.4a is 40 ppm. The estimated TWR error in (4) is at least 20 ns, which corresponds to a pseudorange of almost 6 m at the speed of light. Consequently, the estimated error of TWR cannot be ignored even if e_M and e_B are small.

The basic MCC-TWR process is similar to TWR, except that a relative duration coefficient is introduced. We first obtain the relative duration coefficient by using the first two round trips, then calculate TOF in the first round trip. It is assumed that the ideal parameters duration $T_{\text{dur}}^{\text{MT},1}$ and duration $T_{\text{dur}}^{\text{BS}_i,1}$ satisfy the following time relationship:

$$T_{\text{dur}}^{\text{MT},1} = t_t^{\text{MT},2} - t_t^{\text{MT},1}, \quad T_{\text{dur}}^{\text{BS}_i,1} = t_r^{\text{BS}_i,2} - t_r^{\text{BS}_i,1}. \quad (5)$$

Then, we will obtain the true durations in the MT and BS_i defined as

$$\hat{T}_{\text{dur}}^{\text{MT},1} = (1 + e_M) T_{\text{dur}}, \quad \hat{T}_{\text{dur}}^{\text{BS}_i,1} = (1 + e_B) T_{\text{dur}} \quad (6)$$

where T_{dur} represents the ideal duration. Denote $\eta = \hat{T}_{\text{dur}}^{\text{MT},1}/\hat{T}_{\text{dur}}^{\text{BS}_i,1}$, where η represents the relative duration coefficient.¹ For calculating the relative duration coefficient η , we need to know the duration $\hat{T}_{\text{dur}}^{\text{MT},1}$ between the first transmitting signal and the second transmitting signal at MT,² and the duration $\hat{T}_{\text{dur}}^{\text{BS}_i,1}$ between the first receiving signal and the second receiving signal at BS, as shown in Fig. 1(b). Therefore, adding the second round trip is used to compute $\hat{T}_{\text{dur}}^{\text{MT},1}$ and $\hat{T}_{\text{dur}}^{\text{BS}_i,1}$.

In addition, in our proposed MCC-TWR, the estimated TOF is $\hat{T}_{\text{tow}}^{\text{MT}, \text{MCC-TWR}} = (\hat{T}_{\text{tr}}^{\text{MT},1} - \eta \hat{T}_{\text{rt}}^{\text{BS}_i,1})/2$ in the first round trip,³ where $\hat{T}_{\text{tr}}^{\text{MT},1}$ is true measurement of round-trip timer from the signal transmitting time to the signal receiving time in the first round trip at MT, $\hat{T}_{\text{rt}}^{\text{BS}_i,1}$ is true measurement of round-trip timer from the signal receiving time to the signal transmitting time in the first round trip at BS_i, and η is used to convert the local processing delay of the BS_i to the local clock of MT. Since the time system between BS_i and MT is not synchronized, and the processing delay $\hat{T}_{\text{rt}}^{\text{BS}_i,1}$ is measured in BS_i, we need to facilitate

¹To simplify the description, we have redrawn Fig. 2 to present the relationship between $\hat{T}_{\text{dur}}^{\text{MT},1}$ and $\hat{T}_{\text{dur}}^{\text{BS}_i,1}$ more clearly.

²The duration $\hat{T}_{\text{dur}}^{\text{MT},1}$ between the first transmitting signal from MT and the second transmitting signal is determined by the system setting and can be easily obtained. Similarly, the duration $\hat{T}_{\text{dur}}^{\text{BS}_i,1}$ between the first receiving signal and the second receiving signal at the BS can also be obtained.

³The proposed method combines two round trips, introducing η to reduce time errors caused by clock drifts and improve the precision of $\hat{T}_{\text{rt}}^{\text{BS}_i,1}$ in (3).

the conversion of processing delay $\hat{T}_{\text{rt}}^{\text{BS}_i,1}$ of BS_i to that of MT. The purpose of the conversion is to minimize the impact of BS_i clock drift and asynchronous clocks on TOF estimation. In engineering practice, it is easier to obtain the duration $\hat{T}_{\text{dur}}^{\text{MT},1}$ and $\hat{T}_{\text{dur}}^{\text{BS}_i,1}$, compared with the value of the deviations (e_M or e_B) of some BSs or terminal clocks. Therefore, when calculating η , we take durations into consideration in (5) and (6).

We rewrite η as $\eta = (1 + e_M)/(1 + e_B)$ and obtain the error of MCC-TWR given by

$$\begin{aligned} \text{Error}_{\text{MCC-TWR}} &= \hat{T}_{\text{tow}}^{\text{MT}} - T_{\text{tow}}^{\text{MT}} \\ &= (\hat{T}_{\text{tr}}^{\text{MT}} - \eta \hat{T}_{\text{rt}}^{\text{BS}_i})/2 - (T_{\text{tr}}^{\text{MT}} - T_{\text{rt}}^{\text{BS}_i})/2 \\ &= (1 + e_M)(T_{\text{tr}}^{\text{MT}} - T_{\text{rt}}^{\text{BS}_i})/2 - (T_{\text{tr}}^{\text{MT}} - T_{\text{rt}}^{\text{BS}_i})/2 \\ &= e_M (T_{\text{tr}}^{\text{MT}} - T_{\text{rt}}^{\text{BS}_i})/2 = e_M T_{\text{tow}}^{\text{MT}}. \end{aligned} \quad (7)$$

Given the priority of the time error, $T_{\text{tow}}^{\text{MT}}$ is in the order of nanoseconds; hence, the value of $e_M T_{\text{tow}}^{\text{MT}} = e_M (T_{\text{tr}}^{\text{MT}} - T_{\text{rt}}^{\text{BS}_i})/2$ is almost zero. Ulteriorly, from (4) and (7), it is easy to prove that the proposed method obviously reduces the impact of clock drift on TOF.

The MCC-TWR method introduces a slight increase in overall pseudorange time compared with the traditional TWR method due to an additional round-trip time. However, it is crucial to note that this delay is primarily determined by the pseudorange between the target and the BS. It is important to highlight that the time delay an additional round-trip time is small in practical scenarios. For instance, for a target pseudorange of 1000 m, the time required for a single signal round trip is approximately 2×10^{-5} s. With MCC-TWR, involving two round trips, the total time would be 4×10^{-5} s.

Based on our investigations [27], we have found that the error of the DS-TWR pseudorange method can be approximated by the following equation:

$$\text{Error}_{\text{DS-TWR}} = \frac{T_{\text{tow}}^{\text{MT}}(e_M + e_B)}{2} + \frac{(e_M - e_B)(T_{\text{rt}}^{\text{BS}_i,1} - T_{\text{rt}}^{\text{BS}_i,2})}{4}. \quad (8)$$

Since $T_{\text{rt}}^{\text{BS}_i,1} - T_{\text{rt}}^{\text{BS}_i,2}$ is much larger than $T_{\text{tow}}^{\text{MT}}$, the error in (8) can be simplified to

$$\text{Error}_{\text{DS-TWR}} \approx \frac{(e_M - e_B)(T_{\text{rt}}^{\text{BS}_i,1} - T_{\text{rt}}^{\text{BS}_i,2})}{4}. \quad (9)$$

In the DS-TWR method, the error $\text{Error}_{\text{DS-TWR}}$ is nonnegligible. However, in our proposed method, $T_{\text{tow}}^{\text{MT}}$ is on the order of nanoseconds, resulting in the error $\text{Error}_{\text{MCC-TWR}} = e_M T_{\text{tow}}^{\text{MT}} = \frac{e_M(T_{\text{tr}}^{\text{MT}} - T_{\text{rt}}^{\text{BS}_i})}{2}$ being almost zero. Therefore, our proposed method outperforms the DS-TWR method. Regarding the AltDS-TWR method [27], the error can be expressed as $\text{Error}_{\text{AltDS-TWR}} = e_M T_{\text{tow}}^{\text{MT}} = e_B T_{\text{tow}}^{\text{MT}}$. It can be observed that the error of our proposed method is equal to that of the AltDS-TWR method. However, we have proposed a new method from a different perspective, which achieves the same result with only in the first round trip.

IV. PROPOSED REPF TECHNIQUE FOR GNSS/5G INTEGRATED NAVIGATION

Section III presents a pseudorange measurement method proposed to improve pseudorange accuracy, whereas Section IV

utilizes the pseudorange information obtained from Section III as measurement inputs for the REPF technique to estimate the position. In this section, a GNSS/5G integrated navigation scheme is proposed in 5G ultradense networks using REPF technology. The first part of integrated GNSS/5G positioning is an RPF with pseudorange measurements in LOS/NLOS environment, and GNSS measurements obtained from dynamic single point positioning, whereas the second part is evolutionary PF instead of resampling.

A. RPF of Given Ranging Measurements in Mixed LOS/NLOS and GNSS Measurements

This article evaluates the performance of REPF technologies in 5G ultradense network environments, involving two primary types of BSs: urban macro (UMa) BS and urban micro (UMi) BS. As outlined in [28], scenarios for 5G ultradense networks delineate the simulation methodology established by the 3GPP working group, incorporating predefined environment parameters. Through predetermined network parameters, the simulation aims to conduct a feasibility study on 5G-based localization by generating numerical results with multipath channels. The proposed methods are applicable in various scenarios, particularly in the realm of AGV, pedestrian navigation, and more, to fulfill the requirements for high-precision positioning. For instance, in an urban environment, an AGV equipped with receivers capable of producing pseudorange measurements on cellular BSs and velocities on GNSS satellites can achieve high-precision positioning when cellular signals are obstructed or NLOS occurs, owing to the robustness of the proposed REPF algorithm and the velocities provided by the GNSS receiver.

In the context where an MT moves within the LOS/NLOS environment, consider the scenario where it acquires pseudorange measurements $\mathbf{y}_{\text{MB}} = (d_{\text{MB},t}^1, \dots, d_{\text{MB},t}^M)$ at time t from M BSs in an ultradense 5G network. The MT's state vectors \mathbf{s}_t and \mathbf{n}_t are defining characteristics, where $\mathbf{s}_t = (x_{\text{MT},t}, y_{\text{MT},t})$ represents the 2-D position of the MT, and $\mathbf{n}_t = (s_{\text{MT},t}^1, \dots, s_{\text{MT},t}^M)$ indicates the LOS state in LOS/NLOS. Here, $s_{\text{MT},t}^i = 1$ denotes LOS, and $s_{\text{MT},t}^i = 0$ denotes NLOS. Integrating the state vector and the LOS state enhances the accuracy of the proposed PF for positioning and strengthens its overall robustness. This improvement is particularly beneficial in scenarios involving dense 5G networks.

1) Pseudorange Measurement Model: Given that pseudorange measurements in NLOS scenarios tend to exceed ideal measurements, we formulate the pseudorange measurement model between the MT and BS_i based on the sight state vector $s_{\text{MT},t}^i$

$$d_{\text{MB},t}^i = \bar{d}_{\text{MB},t}^i + v_1^i + (1 - s_{\text{MT},t}^i) \times v_2^i \quad (10)$$

where $\bar{d}_{\text{MB},t}^i$ represents the true pseudorange measurement, v_1^i is presumed to be zero-mean Gaussian noise with a distribution of $\mathcal{N}(0, \sigma_{v_1}^2)$, and v_2^i represents a positive NLOS pseudorange bias induced by the obstruction of the direct path [12]. NLOS is also influenced by the target's position, but the relationship between NLOS and the target's position is challenging to model. Therefore, it is not possible to use NLOS as useful information to aid in location estimation. Instead, it can only be modeled as a positive bias, resulting in a reduction in the accuracy of location estimation [25].

The assumption is made that the LOS states $s_{\text{MT},t}^i$ for different BSs are independent. A crucial consideration is that the sight state undergoes changes with the movement of the MT. For each BS_i , this implies that the sight state of the MT must be continuously updated, as proposed in [29]

$$s_{\text{MT},t}^i = \begin{cases} 1, & \text{if } p(s_{\text{MT},t}^i = 1 | s_{\text{MT},t-1}^i) \times p_t^i > p_{\text{threshold}} \\ 0, & \text{else} \end{cases} \quad (11)$$

where $p_{\text{threshold}}$ represents the NLOS identification threshold. In a 5G environment, we assume continuous movement of the MT, and the current LOS state is not independent of the last state. Specifically, the current LOS state is defined by the combination of the last LOS state and the current observation likelihood. $p(s_{\text{MT},t}^i = 1 | s_{\text{MT},t-1}^i)$ represents the transition probability for forecasting the present LOS state from the previous state using a first-order Markov model, as defined by

$$\begin{cases} p(s_{\text{MT},t}^i = 1 | s_{\text{MT},t-1}^i = 1) = b \\ p(s_{\text{MT},t}^i = 0 | s_{\text{MT},t-1}^i = 1) = 1 - b \\ p(s_{\text{MT},t}^i = 0 | s_{\text{MT},t-1}^i = 0) = b \\ p(s_{\text{MT},t}^i = 1 | s_{\text{MT},t-1}^i = 0) = 1 - b \end{cases} \quad (12)$$

where b signifies the LOS transition probability. The likelihood function for the LOS state is expressed as

$$p_t^i = \begin{cases} \frac{1}{\sqrt{2\pi}\sigma_{v_1^i}} \exp\left(-\frac{(d_{\text{MB},t}^i - \bar{d}_{\text{MB},t}^i)^2}{2\sigma_{v_1^i}^2}\right), & \text{if } (d_{\text{MB},t}^i > \bar{d}_{\text{MB},t}^i) \\ 1, & \text{else} \end{cases} \quad (13)$$

where $\bar{d}_{\text{MB},t}^i = \bar{d}_{\text{MB},t}^i + a$ denotes the true pseudorange.

2) Linear State Transition Model Incorporating GNSS Control: In the RPF, the acquired pseudorange measurements are employed to estimate both the MT position and the LOS states. Consequently, the state updating process is defined as

$$\mathbf{X}(t) = [x_{\text{MT},t}, y_{\text{MT},t}, s_{\text{MT},t}^1, \dots, s_{\text{MT},t}^M]^T \in \mathbb{R}^{2+M}. \quad (14)$$

Taking into account the presence of an input with sampling time Δt , the linear model can be expanded in the following manner:

$$\mathbf{s}_t = \mathbf{I}\mathbf{s}_{t-1} + \mathbf{B}\boldsymbol{\mu}_{t-1} + \mathbf{w}_{t-1} \quad (15)$$

where the input matrix $\mathbf{B} \in \mathbb{R}^{2 \times 2}$ is represented as $\mathbf{I}\Delta t$

$$\mathbf{B} = \begin{bmatrix} \Delta t & 0 \\ 0 & \Delta t \end{bmatrix}. \quad (16)$$

In our case, the linear model can be employed in GNSS/5G integrated navigation, under the condition that $\boldsymbol{\mu}(t-1)$ encompasses external inputs governing the dynamics. Here, the assumed control is the velocity $v_G(t-1)$, representing the velocity of the MT with the GNSS module. The process noise, with dimensions 2×1 , denoted as \mathbf{w}_{t-1} , is presumed to be zero-mean Gaussian noise, adhering to $\mathbf{w}_{t-1} \sim \mathcal{N}(0, \mathbf{Q})$. In this instance, the covariance matrix \mathbf{Q} characterizes the error associated with the state.

While GNSS is indeed popular for providing positioning solutions, our decision to integrate GNSS estimated velocity

instead of position in our proposed method is driven by the following remark.

Remark 1:

- 1) *Improved motion state estimation:* Velocity information provides valuable insights into the target's dynamics and movement patterns, enhancing estimation performance for applications, such as tracking and motion prediction.
- 2) *Reduced reliance on position updates:* In certain scenarios, obtaining accurate and reliable position updates from GNSS can be challenging due to signal blockage, multipath effects, or urban canyon environments. In GNSS positioning, Doppler shift measurements are generally more accurate for velocity updates compared with position updates. This is because Doppler shift measurements provide direct information about the relative velocity between the receiver and the satellite, and they are less affected by various error sources compared to position measurements.
- 3) *Compatibility with existing GNSS systems:* GNSS receivers commonly provide velocity estimates as a standard output, making it readily available for integration into navigation algorithms. Leveraging this existing information enhances our method without imposing additional requirements.
- 4) *Real-time responsiveness:* GNSS estimated velocity is often available at high update rates, matching the GNSS receiver's measurement rate. By utilizing velocity measurements, our proposed method achieves improved real-time responsiveness in dynamic navigation scenarios.

These considerations collectively contribute to the decision to integrate GNSS estimated velocity, leading to enhanced motion state estimation, reduced reliance on position updates, compatibility with existing GNSS systems, and improved real-time performance.

3) REPF for GNSS/5G Integrated Navigation: The significance of GNSS/5G integrated navigation is to estimate a belief, which is a posterior distribution conditioned on the measurements and encompassing the state space. This posterior is typically called the belief and is denoted as

$$\text{bel}(\mathbf{s}_t) = p(\mathbf{s}_t | O_{1:t}^i) \quad \forall i \in \mathcal{M} \quad (17)$$

where $O_{1:t}^i$ represents the measurement information from time instant 1 to t . Two distinct types of measurement information are considered: 1) perceptual measurements, such as pseudorange measurements $d_{\text{MB},t}^i$, and 2) GNSS data $y_{\text{G},t}$, providing information about the velocity. Then, we have

$$\text{bel}(\mathbf{s}_t) = p(\mathbf{s}_t | O_t^i, y_{\text{G},t-1}, O_{t-1}^i, y_{\text{G},t-2}, \dots, O_1^i) \quad \forall i \in \mathcal{M}. \quad (18)$$

To derive a recursive update equation, we observe that (18) can be transformed by Bayes rules into

$$\text{bel}(\mathbf{s}_t) = \frac{p(O_t^i | \mathbf{s}(t), y_{\text{G},t-1}, \dots, O_1^i) p(\mathbf{s}(t) | y_{\text{G},t-1}, \dots, O_1^i)}{p(O_t^i | y_{\text{G},t-1}, \dots, O_1^i)}. \quad (19)$$

Due to the Markov assumption that future measurement information is independent of past measurement information with

knowledge of the current state, the Markov assumption implies

$$p(O_t^i | \mathbf{s}_t, y_{\text{G},t-1}, \dots, O_1^i) = p(O_t^i | \mathbf{s}_t). \quad (20)$$

Thus, (19) can be simplified to

$$\text{bel}(\mathbf{s}_t) = \frac{p(O_t^i | \mathbf{s}_t) p(\mathbf{s}_t | y_{\text{G},t-1}, \dots, O_1^i)}{p(O_t^i | y_{\text{G},t-1}, \dots, O_1^i)}. \quad (21)$$

Equation (21), which is extended by integrating over the state at time $t - 1$ can be expressed in following expression:

$$\text{bel}(\mathbf{s}_t) =$$

$$\frac{p(O_t^i | \mathbf{s}_t) \int p(\mathbf{s}_t | \mathbf{s}_{t-1}, y_{\text{G},t-1}, \dots, O_1^i) p(\mathbf{s}_{t-1} | y_{\text{G},t-1}, \dots, O_1^i) d_{\mathbf{s}_{t-1}}}{p(O_t^i | y_{\text{G},t-1}, \dots, O_1^i)}. \quad (22)$$

Exploit the Markov assumption to simplify the prior information $p(\mathbf{s}_t | \mathbf{s}_{t-1}, y_{\text{G},t-1}, \dots, O_1^i)$ as

$$p(\mathbf{s}_t | \mathbf{s}_{t-1}, y_{\text{G},t-1}, \dots, O_1^i) = p(\mathbf{s}_t | \mathbf{s}_{t-1}, y_{\text{G},t-1}). \quad (23)$$

In order to obtain the following expression (25) by substituting the belief bel into:

$$\text{bel}(\mathbf{s}_t) =$$

$$\frac{p(O_t^i | \mathbf{s}(t)) \int p(\mathbf{s}_t | \mathbf{s}_{t-1}, y_{\text{G},t-1}) p(\mathbf{s}_{t-1} | y_{\text{G},t-1}, \dots, O_1^i) d_{\mathbf{s}_{t-1}}}{p(O_t^i | y_{\text{G},t-1}, \dots, O_1^i)} \quad (24)$$

the recursive expression is derived as

$$\text{bel}(\mathbf{s}_t) = \frac{p(O_t^i | \mathbf{s}_t) \int p(\mathbf{s}_t | \mathbf{s}_{t-1}, y_{\text{G},t-1}) \text{bel}(\mathbf{s}_{t-1}) d_{\mathbf{s}_{t-1}}}{p(O_t^i | y_{\text{G},t-1}, \dots, O_1^i)}. \quad (25)$$

Given a $\text{bel}(\mathbf{s}_{t-1})$, the fundamental concept of the integrated navigation is to find the posterior distribution with measurement information including pseudorange measurements $d_{\text{MB},t}^i$ and GNSS data $y_{\text{G},t}$. The concept behind the PF is to express the belief $\text{bel}(\mathbf{s}_t)$ through a collection of N weighted samples distributed in accordance with $\text{bel}(\mathbf{s}_t)$

$$\text{bel}(\mathbf{s}_t) \approx \left\{ \mathbf{s}_t^j, \omega^j \right\}_{j=1,\dots,N}. \quad (26)$$

Thus, to obtain a sample of the random state \mathbf{s}_t^j , we will sample $\mathbf{s}_t^j \sim p(\mathbf{s}_t | \mathbf{s}_{t-1}^j, y_{\text{G},t-1})$. The pair $\langle \mathbf{s}_t^j, \omega^j \rangle$ follows the distribution

$$q_t = p(\mathbf{s}_t^j | \mathbf{s}_{t-1}^j, y_{\text{G},t-1}) \times \text{bel}(\mathbf{s}_{t-1}^j) \quad (27)$$

where the prior distribution q_t serves the purpose of proposing samples for the intended posterior distribution, as outlined in (24). However, the prior distribution is not equivalent to the desired posterior.

In our scenario, we define the feasible region as the intersection of multiple circular areas, effectively filtering out particles located outside this region. The feasible region is established as follows:

$$D_{\text{NLOS}} = \{ \mathbf{s}_t | \| \mathbf{s}_t - \mathbf{s}_{\text{BS},i} \| \leq d_{\text{MB},t}^i, i = 1, \dots, \mathcal{L} \} \quad (28)$$

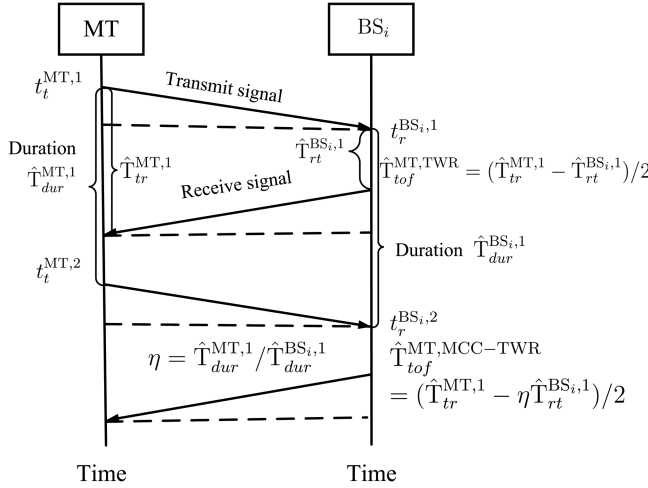


Fig. 2. Relationship between $T_{\text{tof}}^{\text{MT},\text{TWR}}$ and $T_{\text{tof}}^{\text{MT},\text{MCC-TWR}}$.

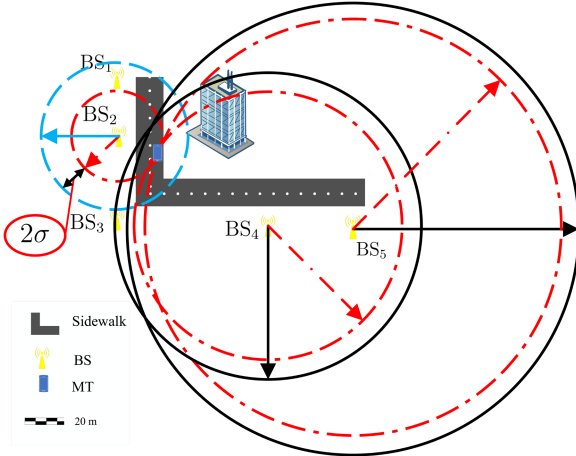


Fig. 3. Scenario of positioning in LOS/NLOS environment.

where s_{BS_i} denotes the position of the BS_i , $\|s_t - s_{\text{BS}_i}\|$ is the Euclidean pseudorange, and \mathcal{L} represents the highest sequence number of the detected NLOS measurements.

The scenario of single MT positioning in LOS/NLOS environment is shown in Fig. 3. In this scenario, solid circles depict the measured pseudoranges, whereas red dashed circles represent the true pseudoranges. Specifically, for LOS measurements, such as those from BS_2 , both the measured and true pseudoranges are indicated by red dashed circles. The feasible region D , comprising NLOS measurements from BS_4 and BS_5 , exhibits considerable size. Consequently, the feasible region D_{LOS} is constructed using LOS measurements, and it is defined as

$$D_{\text{LOS}} = \left\{ s_t \mid \|s_t - s_{\text{BS}_i}\| \leq d_{\text{MB},t}^i + 2\sigma_{v_i^i}, i = 1, \dots, \mathcal{K} \right\} \quad (29)$$

where \mathcal{K} represents the highest sequence number assigned to the detected LOS measurements. As a result, the enhanced feasible region D can be formally expressed as follows:

$$D = D_{\text{NLOS}} \cap D_{\text{LOS}}. \quad (30)$$

The choice to incorporate both LOS and NLOS regions in determining the feasible region stems from two main reasons:

- Utilization of NLOS information:* Unlike traditional methods that discard NLOS measurements, we make effective use of NLOS information. By incorporating NLOS measurements, we enhance the richness of the navigation information, leading to improved accuracy and robustness, especially in challenging urban environments where NLOS conditions are common.
- Realistic representation of practical scenarios:* While an ideal scenario assumes only LOS conditions, real-world scenarios often involve a combination of LOS and NLOS conditions. By considering both LOS and NLOS regions, we account for the presence of NLOS conditions, which are prevalent in practical environments. This realistic representation allows for more reliable navigation solutions by considering all crucial factors that affect positioning accuracy.

Taking into account the improved feasible region D for particle filtering, the particle weights undergo updating as follows:

$$\omega_t^j = \begin{cases} \omega_t^j, & \text{if } (s_t^j \in D) \\ 0, & \text{else.} \end{cases} \quad (31)$$

Express the target distribution for the sample pair $\langle s_t^j, s_{t-1}^j \rangle$ as

$$\text{bel}(s_t^j) = \frac{p(O_t^i | s_t^j)p(s_t^j | s_{t-1}^j, y_{G,t-1})\text{bel}(s_{t-1}^j)}{p(O_t^i | y_{G,t-1}, \dots, O_1^i)}. \quad (33)$$

Following (27), the particle weights (32), as shown at the bottom of the next page, are obtained as the quotient of the desired distribution (33) and the distribution q_t .

As $p(O_t^i | y_{G,t-1}, \dots, O_1^i)$ remains constant, the weights of the particles can be obtained as

$$\omega_t^j = \frac{p(O_t^i | s_t^j)}{p(O_t^i | y_{G,t-1}, \dots, O_1^i)} \propto p(O_t^i | s_t^j). \quad (34)$$

The observation likelihood for the j th particle concerning LOS measurements is represented as

$$p(O_t^i | s_t^j) = \left(\prod_{i=1}^{\mathcal{L}} p_t^{ji} \right)^{\frac{1}{\mathcal{L}}} \quad (35)$$

where p_t^{ji} represents the likelihood of obtaining the measurements $d_{\text{MB},t}^i$ for the j th particle, and we have

$$p_t^{ji} = \frac{1}{\sqrt{2\pi}\sigma_{v_i^i}} \exp \left(-\frac{(d_{\text{MB},t}^i - \tilde{d}_{\text{MB},t}^{ji})^2}{2\sigma_{v_i^i}^2} \right). \quad (36)$$

- New Evolutionary Algorithm Instead of Resampling:* In the conventional PF resampling process, only particles with large weights are duplicated and retained, leading to the elimination of particles with small weights. This approach tends to reduce the diversity of particles, resulting in particle impoverishment. To address this issue, an alternative to resampling is introduced, utilizing a novel evolutionary algorithm. Inspired by genetic algorithms, the proposed evolutionary algorithm incorporates crossover and mutation operations. Through these two operators, the evolutionary algorithm efficiently relocates low-weight particles to regions with a higher likelihood. This strategy aims to

counteract particle impoverishment and maintain a more diverse set of particles in the filtering process.

Following the preceding steps, a set of new particles and their weights is acquired, denoted as $\{\mathbf{s}_t^j, \omega_t^j\}_{j=1,\dots,N}$, where ω_t^j represents the normalized weights. A selection strategy is formulated to distinguish low-weight particles from high-likelihood region particles

$$\mathbf{s}_t^j \in \begin{cases} \mathbf{C}_L, & \text{if } (\omega_t^j \leq \mathcal{W}_{\text{threshold}}) \\ \mathbf{C}_H, & \text{else.} \end{cases} \quad (37)$$

In this context, \mathbf{C}_L and \mathbf{C}_H refer to sets of particles containing low-weight and high-weight particles, respectively. $\mathcal{W}_{\text{threshold}}$ represents the weight threshold used to distinguish particles. The update process is carried out in the following three steps.

- 1) Calculate the effective sample size N_{eff} , and update the effective sample size N_{eff} with given $c = N/2$

$$N_{\text{eff}} = \left[1 / \sum_{i=1}^N (\omega_i^j)^2 \right] \quad (38)$$

where $[.]$ denotes integer ceiling function. In some cases, we find that the effective sample size N_{eff} may be greater than the given particle number N . As a result, in order to avoid overestimation of the algorithm, we restate the effective sample size N_{eff}

$$N_{\text{eff}} = \begin{cases} N_{\text{eff}}, & \text{if } N_{\text{eff}} \leq c \\ c + 1, & \text{else.} \end{cases} \quad (39)$$

- 2) The normalized particle weights ω_t^j are sorted in the descending order and stored in \mathcal{W}_t^j as $\mathcal{W} = \{\mathcal{W}_t^1, \dots, \mathcal{W}_t^N\}$.

3) The threshold $\mathcal{W}_{\text{threshold}}$ is denoted as $\mathcal{W}_{\text{threshold}} = \mathcal{W}_t^{N_{\text{eff}}}$.

Assume that $\mathbf{s}_{L,t}^n (n = 1, \dots, N_L)$ and $\mathbf{s}_{H,t}^h (h = 1, \dots, N_H)$ denote the particles from \mathbf{C}_L and \mathbf{C}_H , where N_L and N_H are denoted as the numbers of the particles contained in \mathbf{C}_L and \mathbf{C}_H , respectively, and the modified low-weight particle is represented as $\mathbf{s}_{M,t}^n$. The arithmetic crossover operator is derived as

$$\mathbf{s}_{M,t}^n = \xi \mathbf{s}_{L,t}^n + (1 - \xi) \mathbf{s}_{H,t}^h \quad (40)$$

where ξ is a number randomly generated in $[0, 1]$, which will diversify the search directions and explore a wider area of the posterior probability density space.

The next operation is the mutation process. Considering that particles $\mathbf{s}_{M,t}^n$ with low weights in \mathbf{C}_L have been updated, the corresponding weights $\mathcal{W}_{\mathbf{C}_L}$ should also be updated. The upper and lower boundaries of particles $\mathbf{s}_{M,t}^n$ with low weights $\mathcal{W}_{\mathbf{C}_L}$

Algorithm 1: Proposed REPF Method for GNSS/5G C Integrated Navigation.

Input: The initial distribution at time $t = 0$.
Output: The posterior location estimation \mathbf{s}_t .

- 1: Sample $\mathbf{s}_0^j \sim \text{bel}(\mathbf{s}_0)$ from the weighted sample set representing $\text{bel}(\mathbf{s}_0)$. Each sample particle \mathbf{s}_0^j is distributed according to the belief distribution $\text{bel}(\mathbf{s}_0)$.
- 2: **for** $t = 1, 2, 3, \dots$ **do**
- 3: Sample $\mathbf{s}_t^j \sim p(\mathbf{s}_t | \mathbf{s}_{t-1}, y_{G,t-1}) \times \text{bel}(\mathbf{s}_{t-1})$ according to (27).
- 4: Estimate the sight state $s_{MB,t}^i$ according to (9)–(11).
- 5: Update the importance weights $\omega^j \propto p(O_t^i | \mathbf{s}_t)$ according to (26)–(32).
- 6: Calculate and update the low-weight particles $\mathbf{s}_{M,t}^n$ according to (34)–(40).
- 7: Integrate all particles (low-weight ones and high-weight ones) and calculate the final filtering result \mathbf{s}_t .
- 8: **end for**

in \mathbf{C}_L are denoted as

$$\mathbf{s}_{U,t}^n = \begin{cases} \mathbf{s}_{M,t}^n + \sigma_{\mathbf{s}_{M,t}^n}, & \text{if } 2 \times p(O_t^i | \mathbf{s}_{M,t}^n) \geq p(O_t^i | \mathbf{s}_{M,t}^{\max}) \\ \mathbf{s}_{M,t}^{\max} + \sigma_{\mathbf{s}_{M,t}^n}, & \text{else} \end{cases} \quad (41)$$

$$\mathbf{s}_{L,t}^n = \begin{cases} \mathbf{s}_{M,t}^n - \sigma_{\mathbf{s}_{M,t}^n}, & \text{if } 2 \times p(O_t^i | \mathbf{s}_{M,t}^n) < p(O_t^i | \mathbf{s}_{M,t}^{\max}) \\ \mathbf{s}_{M,t}^{\max} - \sigma_{\mathbf{s}_{M,t}^n}, & \text{else} \end{cases} \quad (42)$$

where $\sigma_{\mathbf{s}_{M,t}^n}$ denotes the standard deviation of the particles set $\mathbf{s}_{M,t}^n$, and $\mathbf{s}_{M,t}^{\max}$ is the particle with the highest weight in $\mathcal{W}_{\mathbf{C}_L}$.

The updated particle from the high-likelihood region is

$$\mathbf{s}_{M,t}^n = \mathbf{s}_{L,t}^n + (\mathbf{s}_{U,t}^n - \mathbf{s}_{L,t}^n)\phi \quad (43)$$

where ϕ denotes a number randomly generated in $[0, 1]$. Update resulting particles $\mathbf{s}_{M,t}^n$ with the weights $\mathcal{W}_{\mathbf{C}_L}$; as a result, the low-weight particles are moved to high-likelihood region. The proposed REPF technique for GNSS/5G integrated navigation is as shown in Algorithm 1.

5) Complexity Analysis of the REPF: In this section, the computational complexity of the REPF is evaluated via the number of floating-point operations (flops) used in the algorithm. According to Algorithm 1, at time t , the coefficient c_1 is used for the calculation of the Gaussian likelihood, c_2 for the new evolutionary algorithm, c_3 for the Gaussian random number complexity, and c_4 for uniformly distributed random number complexity. In Row 1 of Algorithm 1, equivalent flop (EF) complexity to generate N particles and obey a uniform distribution is $2c_4N$. In Row 3 of Algorithm 1, EF complexity for particles update is $2c_3N$. In Row 4 of Algorithm 1, EF

$$\frac{p(O_t^i | \mathbf{s}_t^j) p(\mathbf{s}_t^j | \mathbf{s}_{t-1}^j, y_{G,t-1}) \text{bel}(\mathbf{s}_{t-1}^j)}{p(O_t^i | y_{G,t-1}, \dots, O_1^i) q_t} = \frac{p(O_t^i | \mathbf{s}_t^j) p(\mathbf{s}_t^j | \mathbf{s}_{t-1}^j, y_{G,t-1}) \text{bel}(\mathbf{s}_{t-1}^j)}{p(O_t^i | y_{G,t-1}, \dots, O_1^i) p(\mathbf{s}_t^j | \mathbf{s}_{t-1}^j, y_{G,t-1}) \times \text{bel}(\mathbf{s}_{t-1}^j)} = \frac{p(O_t^i | \mathbf{s}_t^j)}{p(O_t^i | y_{G,t-1}, \dots, O_1^i)} \quad (32)$$

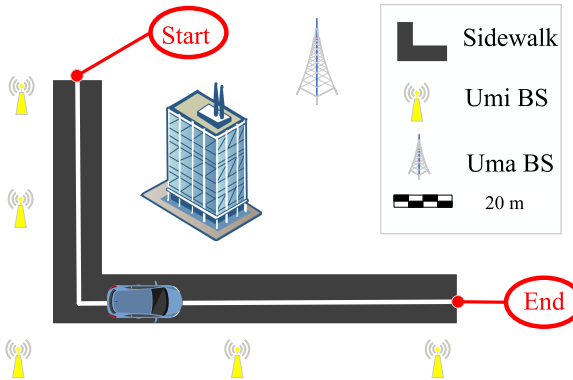


Fig. 4. Mixed UMi-street and UMa-street scenarios with the MT trajectory and multiple BSs.

complexity to estimate the sight state is $N\mathcal{M}$. In Row 5 of Algorithm 1, EF complexity to update the importance weights is $(c_1 + 1)N$. In Rows 6 and 7 of Algorithm 1, EF complexity for the new evolutionary algorithm is $2c_2N$. Hence, the total EF complexity is given by

$$\mathcal{C}(N) = (c_1 + 2c_2 + 2c_3 + 2c_4 + \mathcal{M} + 1)N. \quad (44)$$

We see that the computational complexity of the proposed algorithm does not increase significantly compared with the standard PF algorithm, and the computational complexities of them are equal to $\mathcal{O}(N)$.

Remark 2: If the number of particles in a PF or REPF is significantly larger than the dimensionality of the state for low-dimensional problems, the computational complexity of the PF would be higher compared with the interacting multiple model-extended Kalman filter (IMM-EKF). This is because the PF's complexity is linear with respect to the number of particles, while the IMM-EKF's complexity is typically cubic with respect to the state dimension. Therefore, even with a low-dimensional state, the computational overhead of processing a large number of particles in the PF can outweigh the operations performed by the IMM-EKF, resulting in higher complexity. In practice, an appropriate number of particles are usually selected to maintain better real-time performance.

V. SIMULATION

In this section, we conduct comprehensive numerical evaluations to demonstrate and quantify the performance of GNSS/5G integrated navigation using the proposed methods in 5G ultra-dense networks. Fig. 4 depicts the UMi-street and UMa-street scenarios with a single MT trajectory and BSs in 5G environment, covering a deployment area of $60\text{ m} \times 110\text{ m}$. To present simulation results, we assess the performance with a dataset of generated GNSS and 5G data. The GNSS data are simulated by introducing Gaussian noises to a constant velocity $v_G = 1\text{ m/s}$, while 5G data are generated with additional measurement noises [cf., (45)] and NLOS bias modeled according to (47). The noise distribution of the GPS receiver is determined by a GPS receiver module, specifically, the Garmin GPS 18x-5 Hz. The specifications include a position error $2\sigma_{\text{gnss}} < 15\text{ m}$ (where σ_{gnss} is the standard deviation of the positioning), a velocity error of 0.1 knot, and a frequency of 5 Hz [30].

While it is true that GNSS velocity estimation is based on Doppler shift measurements, which can be affected by reflections and introduce bias, modeling the velocity error with a normal distribution can still be a reasonable approximation for several reasons.

- 1) *Aggregation of multiple measurements:* In practical GNSS systems, velocity estimation involves collecting multiple Doppler shift measurements over a certain time window. By considering the combined effect of these measurements, the resulting velocity error tends to exhibit characteristics that can be approximated by a normal distribution, especially when a sufficient number of measurements are used.
- 2) *Central limit theorem:* The central limit theorem asserts that the sum or average of a sufficiently large number of independent and identically distributed random variables tends to converge to a normal distribution. In the context of GNSS velocity estimation, the Doppler shift measurements can be seen as independent and identically distributed random variables. Their summation or averaging can lead to a distribution that approaches a normal distribution, providing a valid approximation for the velocity error.
- 3) *Simplifying assumption:* By modeling the velocity error with a normal distribution, we establish a practical and mathematically tractable framework to analyze and characterize the proposed algorithm's performance. While acknowledging that this approach may not fully account for the complexity of biases introduced by reflections in urban areas, it offers a reasonable simplification, enabling us to evaluate the overall system performance and compare various algorithms and techniques. An example demonstrating the use of this approach can be found in [31], where the authors present the NaveGo simulation framework for low-cost GNSS/IMU integrated navigation systems, utilizing a normal distribution to model the GNSS velocity error.

By considering these factors, modeling GNSS velocity error with a normal distribution offers a reasonable approximation that enables analysis, evaluation, and comparison of the proposed algorithm's performance. It acknowledges the challenges posed by reflections in urban areas while providing a practical framework for assessing the system's overall accuracy and robustness.

This section compares four algorithms: the IMM-EKF [32], the PF, the robust evolutionary particle filter (REPF) using 5G cellular signals, and GNSS. In the context of 5G systems, concerning the OFDM signal, the variance⁴ of v_1^i can be calculated by

$$\sigma_{v_1^i}^2 = \text{var}(v_1^i) = \frac{c^2 T_s^2}{8\pi^2 \cdot \text{SNR}_i \cdot \sum_{n \in \mathcal{N}_{\text{PRS}}} p_n^2 \cdot n^2} \quad (45)$$

where c denotes the velocity of electromagnetic waves, T_s represents the OFDM symbol duration ($T_s = \frac{1}{F_{\text{sc}}}$), \mathcal{N}_{PRS} refers to the subset of subcarriers dedicated to the positioning reference

⁴According to [33], (45) is obtained from the Cramér–Rao lower bound (CRLB) of the time delay estimation. In [33], the CRLB of the TOA estimation was derived rigorously by directly using discrete Fourier transform.

signal (PRS), and p_n^2 signifies the relative power weight assigned to the n th subcarrier.

The assessment of error statistics is conducted in the presence of multipath conditions. The channel impulse response (CIR) is simulated using ray tracing, as described in [25]. The simulated CIR is represented by a generic model, formulated as

$$h(\tau) = \sum_{l=0}^{L-1} \alpha_l \delta(\tau - \tau_l) \quad (46)$$

where L representing the count of multipath components, α_l and τ_l denote the relative attenuation and delay components of the l th path concerning the first path. Subsequently, the NLOS bias term v_2^i can be forecasted using the simulated CIR and is articulated as per the work by Shamaei and Kassas [25]

$$v_2^i = \frac{c(\sin(\frac{\pi}{2N_a}))^3}{4\pi F_{sc} \cos(\frac{\pi}{2N_a})} (\chi_1 + \chi_2) \quad (47)$$

where N_a represents the count of active subcarriers, and χ_1 and χ_2 signify the biases associated with multipath effects, as detailed in [25]. These biases are contingent upon the geometric characteristics of the CIR. In [25], two more realistic CIRs (i.e., different fading channels) are considered and the statistics of the multipath bias are compared for different numerologies.

A. Path Loss

Two multifrequency PL models are under consideration in 5G ultradense network scenarios: the close-in free space reference pseudorange PL model and the Alpha–Beta–Gamma (ABG) PL model. The existing PL models in the 3GPP 3-D model adhere to the ABG model but do not incorporate a frequency-dependent parameter (AB model). Moreover, these models introduce additional considerations related to the height of BSs or terminals and incorporate a LOS breakpoint. In this article, the multifrequency ABG PL model from [34] is adopted

$$\begin{aligned} \text{PL}_{\text{ABG}}(f, d)[\text{dB}] \\ = 10\alpha \log_{10}(d_{\text{MB}}) + \beta + 10\gamma \log_{10}(f) + X_{\sigma}^{\text{ABG}} \end{aligned} \quad (48)$$

where f denotes the frequency measured in GHz, α quantifies the rise in PL with the expansion of the transmit–receive pseudorange, β represents a variable offset value in dB, γ aims to address the variation of PL concerning the frequency f in GHz, and X_{σ}^{ABG} stands for the Shadow Fading (SF) term, which adheres to a log-normal distribution with a standard deviation of σ_{SF} in dB.

B. SNR and SINR

The PL is defined as [33]

$$L_i[\text{dB}] = \max(\text{PL}_{\text{ABG}}(f, d_{\text{MB}}^i)) - G_{rx}, \text{MCL} \quad (49)$$

where G_{rx} denotes the gain of the receiver antenna, and MCL refers to the minimum coupling loss (MCL). The formulation of the received signal power is represented as follows:

$$C_i = P_{\text{max}} - L_i - \text{SF}. \quad (50)$$

The resulting C/N_0 observed at the output of the receiver's radio frequency front-end is

$$(C/N_0)_i = C_i - N_0 - \text{NF} \quad (51)$$

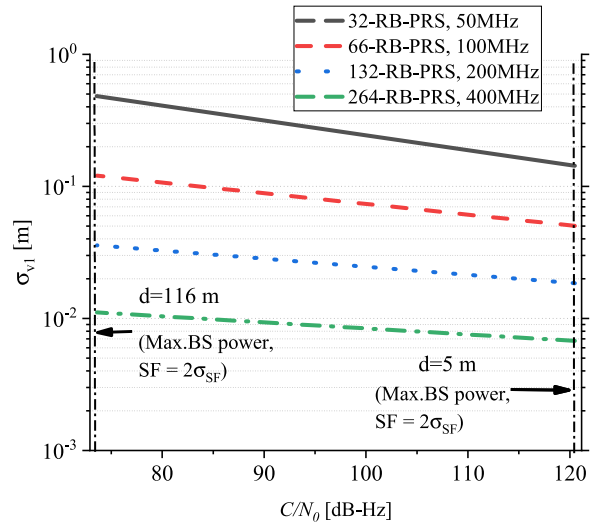


Fig. 5. Graphing σ_{v_1} against the carrier-to-noise ratio C/N_0 involves employing various 5G system bandwidths and taking into account the potential range of C/N_0 within the context of 5G ultradense networks.

where N_0 represents the noise spectral density, approximately equivalent to -174 dBm/Hz, and NF denotes the receiver noise figure. The SNR for the signal received from the i th BS is expressed as

$$\text{SNR}_i = (C/N_0)_i - 10 \cdot \log_{10}(B) \quad (52)$$

where the bandwidth of the multicarrier signal is denoted as $B = N_a \cdot F_{sc}$, where in LTE, $N_a = 12 \cdot N_{\text{RB}} - 4$ represents the number of active subcarriers, and there are $N_{\text{PRS}} = 2 \cdot N_{\text{RB}}$ scattered PRS pilots. The subcarrier spacing is defined as $F_{sc} = 120$ kHz.

The interference between BSs becomes nonnegligible, especially when having a large number of BSs. Therefore, to include the interference, the performance metric of the SINR is considered at the i th BS instead of SNR and is given by

$$\text{SINR}_i = \frac{P_{rx,i}}{\sum_{j \neq i} P_{rx,j} + N_{rx}} \quad (53)$$

where $P_{rx,j}$ represents the received interference power from the j th BS at the i th BS, and N_{rx} denotes the receiver noise floor.

C. Simulating 5G Ultradense Network Environments

Fig. 5 exhibits a graphical representation illustrating the relationship between σ_{v_1} and the carrier-to-noise ratio C/N_0 across varying 5G system bandwidths. This exploration takes into consideration the potential range of C/N_0 within the context of the 5G ultradense network scenario. Defining the C/N_0 thresholds for two fundamental network designs with high and low intersite pseudoranges (ISD), specifically d_{MB} values of 116 and 5 m, respectively, is crucial. The 5G ultradense network scenarios adhere to predefined parameters outlined in Table I. In the initial scenario, where maximum path losses are assumed, the path attenuation is approximately 132.59 dB for $d_{\text{MB}} = 120$ m at $f = 30$ GHz. By utilizing $P_{\text{max}} = 43$ dBm and $\text{SF} = 2\sigma_{\text{SF}}$, the C/N_0 threshold is 72.91 dB-Hz. This threshold imposes a limitation, allowing the achievement of a targeted accuracy of 30 cm only with a signal bandwidth exceeding 50 MHz. In the second scenario, considering minimum path losses, the path

TABLE I
ENVIRONMENT PARAMETERS OF THE 5G ENVIRONMENT

Parameters [28]	Value		Parameters [28]	Value	
	UMi	UMa		UMi	UMa
α	3.48	3.4	P_{max}	47 dBm	47 dBm
β	21.02	19.2	SF	$2\sigma_{SF}$	$2\sigma_{SF}$
γ	2.34	2.3	N_0	-174 dBm/Hz	-174 dBm/Hz
σ_{SF}	6.5 dB	6.5 dB	Bandwidth	100 MHz	25 MHz
f	30 GHz	3 GHz	N_{RB}	66	65
G_{rx}	0 dBi	0 dBi	Subcarrier spacing	120 kHz	30 kHz
MCL	70	70	N_{PRS}	132	130
NF	9 dB	9 dB	N_a	788	776

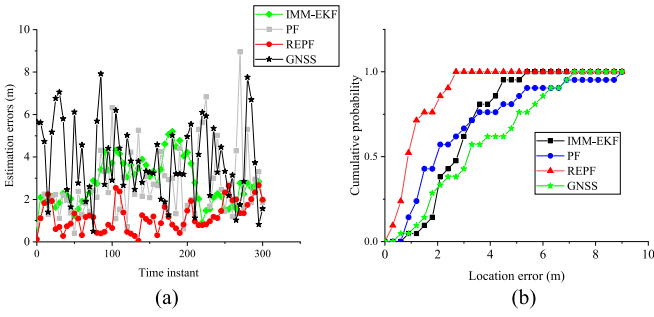


Fig. 6. Localization error analysis. (a) Localization error along the path. (b) CDF of localization error.

attenuation is around 83.75 dB for $d_{MB} = 5$ m at $f = 30$ GHz, using the PL model specific to ultradense network scenarios [34]. Consequently, with $P_{max} = 43$ dBm and SF = $2\sigma_{SF}$, the C/N_0 threshold is 121.15 dB-Hz. This indicates that the target accuracy can be achieved with any signal bandwidth. Both of these C/N_0 thresholds are visually represented in Fig. 5.

Fig. 6(a) illustrates the localization error along the path, whereas Fig. 6(b) presents the cumulative distribution function (CDF) of this error. Analysis of these figures reveals that even in the challenging conditions of LOS/NLOS within 5G ultradense network scenarios, the proposed REPF algorithm achieves remarkable positioning accuracy at the 1-m level. This success is attributed to the construction of an effective LOS/NLOS feasible region for particle filtering and the incorporation of a cutting-edge evolutionary algorithm. In the assessment of positioning performance, IMM-EKF demonstrates superiority over PF. The fundamental principle of IMM theory revolves around the seamless integration of LOS and NLOS switching. As a result, the challenge of mobile location estimation undergoes a transformation into a nonlinear filtering process applied to jump Markov systems featuring two independent switching parameters. This transformation enhances the robustness of IMM-EKF compared with PF, especially in the intricate mixed LOS/NLOS environment.

The obtained positioning results from the comprehensive numerical evaluations are depicted in Fig. 7(a). Observations from Fig. 7(a) indicate an enhancement in positioning performance when pseudorange measurements are integrated from a greater number of BSs in comparison to scenarios with fewer BSs. Despite the interference among BSs, the incorporation of more

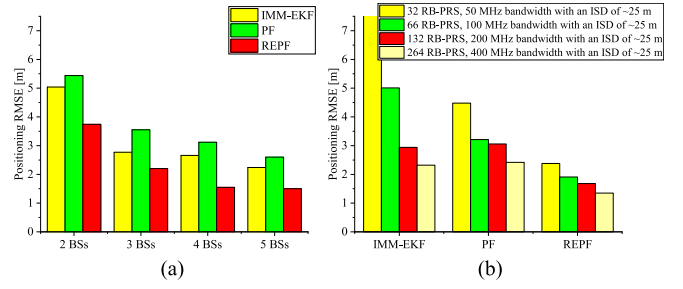


Fig. 7. RMSE examination. (a) Evaluation of RMSE across various positioning techniques with varying BS quantities. (b) Assessment of RMSE for all positioning methods under diverse simulation numerologies, maintaining an ISD of 25 m.

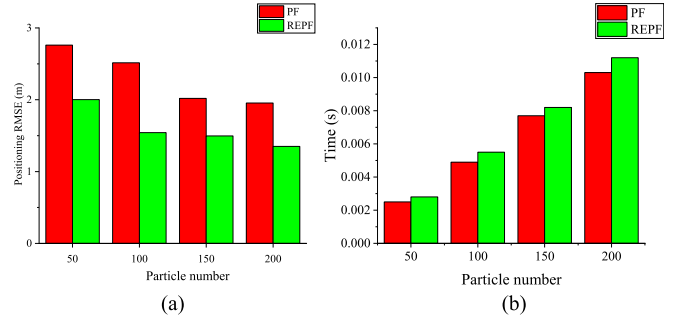


Fig. 8. Positioning RMSE and processing time. (a) Impact of particle number on GNSS/5G integrated navigation RMSE. (b) Impact of particle number on GNSS/5G integrated navigation processing time.

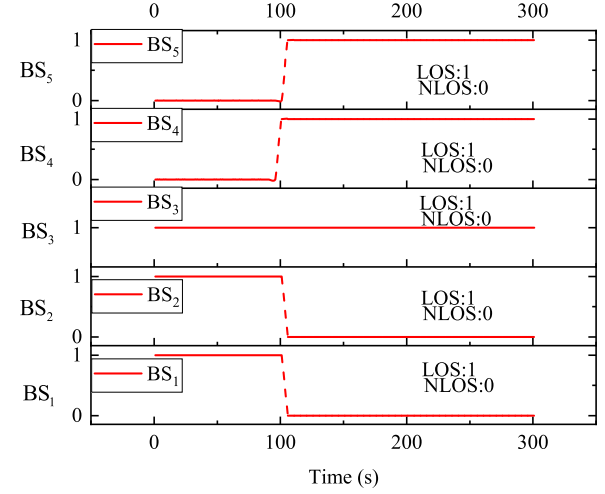


Fig. 9. States of sight along the trajectory.

effective observations proves beneficial for refining positioning accuracy. Fig. 7(b) presents RMSEs for all positioning methods across diverse simulation numerologies, maintaining an ISD of 25 m. It is evident that owing to the larger transmission bandwidth associated with higher N_{RB} , the standard deviation of measurement noise error is notably lower by two orders of magnitude compared with cases with lower N_{RB} . Table I tabulates comparison of localization error, where the detailed statistical characters about the median, average, standard deviation, maximum, and RMSEs of the localization error are summarized. Based on the obtained positioning results that are

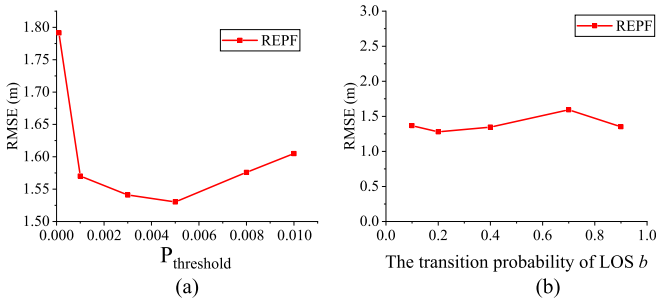


Fig. 10. Sensitivity analysis of different parameters: (a) Impact of $P_{\text{threshold}}$ on the REPF algorithm. (b) Impact of the transition probability of LOS b on the REPF algorithm.

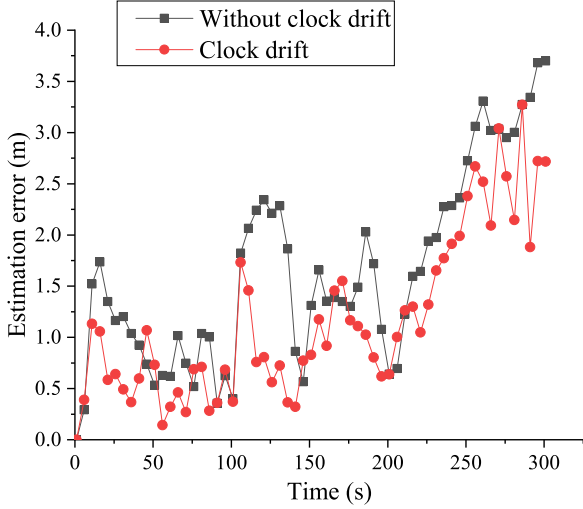


Fig. 11. Impact of clock drift on the REPF algorithm.

TABLE II

COMPARISON OF LOCALIZATION ERROR: 66 RB-PRS, 100 MHz BANDWIDTH WITH AN ISD OF 25 M

Algorithm	Max (m)	Mean (m)	Median (m)	Std (m)	RMSE (m)
GNSS	14.22	3.74	3.51	1.88	4.18
IMM-EKF	5.22	2.74	2.62	1.00	2.91
PF	12.80	2.71	2.10	2.00	3.33
REPF	2.92	1.20	1.04	0.68	1.32

illustrated in Fig. 7 and Table II, the proposed REPF significantly outperforms the earlier proposed IMM-EKF and PF in all considered evaluation scenarios. Fig. 8 shows the impact of the particle number on the positioning RMSE and processing time. The simulation is implemented on Dell laptop with CPU Intel Core i7 and 16 GB RAM. It is observed that with the increasing of particle number, the RMSEs of PF and the proposed algorithm become lower, and the processing time of the proposed algorithm becomes longer. It is also shown that processing time of the proposed algorithm is close to the PF.

The states of sight along the trajectory are shown in Fig. 9. The number 0 denotes the state of sight NLOS, whereas the number 1 represents the state of sight LOS. In particularly, the MT is always in LOS with respect to the BS₃. The sensitivity analysis of different parameters, including the sight state transition probability of LOS b and $p_{\text{threshold}}$, is shown in Fig. 10. The

RMSEs are analyzed with the changes of the two parameters. From Fig. 10(a), it is observed that the REPF algorithm performs best when $p_{\text{threshold}} = 0.005$. Fig. 10(b) shows that the impact on the sight state transition probability of LOS b is maintained at a limited level on the REPF algorithm. From Fig. 11, it is shown that as the MCC-TWR scheme can reduce the effect of the clock drift, the proposed REPF algorithm considering the clock drift performs better than the REPF algorithm by ignoring the clock drift.

VI. CONCLUSION

This article focuses on achieving high-efficiency GNSS/5G integrated navigation within 5G ultradense networks. We introduced an REPF technique for state estimation. Initially, an MCC-TWR scheme in 5G ultradense networks was proposed to enhance pseudorange accuracy compared with traditional two-way pseudorange. Subsequently, we established the posterior belief conditioned on given pseudorange measurements and GNSS velocity. Building upon this posterior distribution, an RPF algorithm, tailored for LOS/NLOS environments, was introduced to estimate the MT's sight state and position. To address potential particle degradation in the robust algorithm, a novel evolutionary algorithm based on genetic theory was introduced to augment the diversity of particle filtering. Comprehensive performance evaluations within 5G ultradense networks, incorporating a movement model based on given pseudorange measurements and GNSS velocity, clearly demonstrate the capability of achieving meter-scale positioning and tracking accuracy for the moving MT in LOS/NLOS environments using the proposed REPF technique. It is worth noting that, although designed for 5G scenarios, our proposed method can be extended to applications such as radar and (UWB TOA positioning. However, it is essential to acknowledge that this particle filtering-based method has limitations. While robust, the selection of the number of particles is environment dependent, and its real-time performance may not be as immediate as methods like EKF.

REFERENCES

- [1] K. Wen, K. Yu, Y. Li, S. Zhang, and W. Zhang, "A new quaternion Kalman filter based foot-mounted IMU and UWB tightly-coupled method for indoor pedestrian navigation," *IEEE Trans. Veh. Technol.*, vol. 69, no. 4, pp. 4340–4352, Apr. 2020.
- [2] Y. Zhang, X. Tan, and C. Zhao, "UWB/INS integrated pedestrian positioning for robust indoor environments," *IEEE Sens. J.*, vol. 20, no. 23, pp. 14401–14409, Dec. 2020.
- [3] F. Tong, Y. Sun, and S. He, "On positioning performance for the narrow-band Internet of Things: How participating eNBs impact?," *IEEE Trans. Ind. Inform.*, vol. 15, no. 1, pp. 423–433, Jan. 2019.
- [4] B. Panchal, K. Subramanian, and S. E. Talole, "Robust missile autopilot design using two time-scale separation," *IEEE Trans. Aerosp. Electron. Syst.*, vol. 54, no. 3, pp. 1499–1510, Jun. 2018, doi: 10.1109/TAES.2018.2796654.
- [5] B. Kürkçü and C. Kasnakoglu, "Robust autopilot design based on a disturbance/uncertainty/coupling estimator," *IEEE Trans. Control Syst. Technol.*, vol. 27, no. 6, pp. 2622–2629, Nov. 2019.
- [6] C. Huang et al., "Machine learning-enabled LOS/NLOS identification for: MIMO systems in dynamic environments," *IEEE Trans. Wireless Commun.*, vol. 19, no. 6, pp. 3643–3657, Jun. 2020.
- [7] N. Zhu, J. Marais, D. Bétaillie, and M. Berbineau, "GNSS position integrity in urban environments: A review of literature," *IEEE Trans. Intell. Transp. Syst.*, vol. 19, no. 9, pp. 2762–2778, Sep. 2018.

- [8] M. Witrisal et al., "High-accuracy localization for assisted living: 5G systems will turn multipath channels from foe to friend," *IEEE Signal Process. Mag.*, vol. 33, no. 2, pp. 59–70, Mar. 2016.
- [9] C. Koivisto et al., "Joint device positioning and clock synchronization in 5G ultra-dense networks," *IEEE Trans. Wireless Commun.*, vol. 16, no. 5, pp. 2866–2881, May 2017.
- [10] F. Wen, J. Kulmer, K. Witrisal, and H. Wymeersch, "5G positioning and mapping with diffuse multipath," *IEEE Trans. Wireless Commun.*, vol. 20, no. 2, pp. 1164–1174, Feb. 2021, doi: [10.1109/TWC.2020.3031180](https://doi.org/10.1109/TWC.2020.3031180).
- [11] H. Kim, K. Granstrom, L. Gao, G. Battistelli, S. Kim, and H. Wymeersch, "5G mmWave cooperative positioning and mapping using multi-model PHD filter and map fusion," *IEEE Trans. Wireless Commun.*, vol. 19, no. 6, pp. 3782–3795, Jun. 2020, doi: [10.1109/TWC.2020.2978479](https://doi.org/10.1109/TWC.2020.2978479).
- [12] O. Kanhere and T. S. Rappaport, "Position location for futuristic cellular communications: 5G and beyond," *IEEE Commun. Mag.*, vol. 59, no. 1, pp. 70–75, Jan. 2021, doi: [10.1109/MCOM.001.2000150](https://doi.org/10.1109/MCOM.001.2000150).
- [13] L. Yin, Q. Ni, and Z. Deng, "A GNSS/5G integrated positioning methodology in D2D communication networks," *IEEE J. Sel. Areas Commun.*, vol. 36, no. 2, pp. 351–362, Feb. 2018.
- [14] L. Gazzah and L. Najjar, "Enhanced cooperative group localization with identification of LOS/NLOS BSs in 5G dense networks," *Ad Hoc Netw.*, vol. 89, pp. 88–96, 2019.
- [15] S.-C. Lin and I. F. Akyildiz, "Dynamic base station formation for solving NLOS problem in 5G millimeter-wave communication," in *Proc. IEEE INFOCOM, IEEE Conf. Comput. Commun.*, 2017, pp. 1–9.
- [16] Y. Wang, K. Gu, Y. Wu, W. Dai, and Y. Shen, "NLOS effect mitigation via spatial geometry exploitation in cooperative localization," *IEEE Trans. Wireless Commun.*, vol. 19, no. 9, pp. 6037–6049, Sep. 2020, doi: [10.1109/TWC.2020.2999667](https://doi.org/10.1109/TWC.2020.2999667).
- [17] Z. Yuan, W. Rui, and X. Zhe, "Collaborative navigation in urban environments via GNSS and 5G signals," in *Proc. IEEE Int. Conf. Commun.*, 2023, pp. 6275–6280.
- [18] N. Kbayr and M. Sahmoudi, "Performances analysis of GNSS NLOS bias correction in urban environment using a three-dimensional city model and GNSS simulator," *IEEE Trans. Aerosp. Electron. Syst.*, vol. 54, no. 4, pp. 1799–1814, Aug. 2018.
- [19] N. Viandard, D. Nahimana, J. Marais, and E. Duflos, "GNSS performance enhancement in urban environment based on pseudo-range error model," in *Proc. IEEE/ION Position, Location Navigation Symp.*, 2008, pp. 377–382.
- [20] J. Lesouape, T. Robert, M. Sahmoudi, J.-Y. Tourneret, and W. Vigneau, "Multipath mitigation for GNSS positioning in an urban environment using sparse estimation," *IEEE Trans. Intell. Transp. Syst.*, vol. 20, no. 4, pp. 1316–1328, Aug. 2019.
- [21] A. Kumar and A. K. Singh, "A novel multipath mitigation technique for GNSS signals in urban scenarios," *IEEE Trans. Veh. Technol.*, vol. 69, no. 3, pp. 2649–2658, Mar. 2020.
- [22] L.-T. Hsu, S.-S. Jan, P. D. Groves, and N. Kubo, "Multipath mitigation and NLOS detection using vector tracking in urban environments," *GPS Solutions*, vol. 19, pp. 249–262, 2015.
- [23] M. Maaref and Z. M. Kassas, "Ground vehicle navigation in GNSS-challenged environments using signals of opportunity and a closed-loop map-matching approach," *IEEE Trans. Intell. Transp. Syst.*, vol. 21, no. 7, pp. 2723–2738, Jul. 2020.
- [24] S. Ragotthaman, M. Maaref, and Z. M. Kassas, "Autonomous ground vehicle path planning in urban environments using GNSS and cellular signals reliability maps: Models and algorithms," *IEEE Trans. Aerosp. Electron. Syst.*, vol. 57, no. 3, pp. 1562–1580, Jun. 2021.
- [25] K. Shamaei and Z. M. Kassas, "Receiver design and time of arrival estimation for opportunistic localization with 5G signals," *IEEE Trans. Wireless Commun.*, vol. 20, no. 7, pp. 4716–4731, Jul. 2021.
- [26] L. Chen, X. Zhou, F. Chen, L.-L. Yang, and R. Chen, "Carrier phase ranging for indoor positioning with 5G NR signals," *IEEE Internet Things J.*, vol. 9, no. 13, pp. 10908–10919, Jul. 2022.
- [27] D. Neirynck, E. Luk, and M. McLaughlin, "An alternative double-sided two-way ranging method," in *Proc. 13th Workshop Positioning, Navigation Commun.*, 2016, pp. 1–4.
- [28] 3GPP, "Study on NR positioning support," 3GPP, Sophia Antipolis, France, Tech. Rep. 38.855, 2019.
- [29] J. Wang, Q. Gao, Y. Yu, H. Wang, and M. Jin, "Toward robust indoor localization based on Bayesian filter using chirp-spread-spectrum ranging," *IEEE Trans. Ind. Electron.*, vol. 59, no. 3, pp. 1622–1629, Mar. 2012.
- [30] S. K. Rechcemmer et al., "Utilization of smartphone data for driving cycle synthesis based on electric two-wheelers in Shanghai," *IEEE Trans. Intell. Transp. Syst.*, vol. 22, no. 2, pp. 876–886, Feb. 2021.
- [31] R. Gonzalez, J. I. Giribet, and H. D. Patino, "NaveGo: A simulation framework for low-cost integrated navigation systems," *J. Control Eng. Appl. Inform.*, vol. 17, no. 2, pp. 110–120, 2015.
- [32] W. Li and Y. Jia, "Location of mobile station with maneuvers using an IMM-based cubature Kalman filter," *IEEE Trans. Ind. Electron.*, vol. 59, no. 11, pp. 4338–4348, Nov. 2012, doi: [10.1109/TIE.2011.2180270](https://doi.org/10.1109/TIE.2011.2180270).
- [33] J. A. d. Peral-Rosado, J. A. López-Salcedo, S. Kim, and G. Seco-Granados, "Feasibility study of 5G-based localization for assisted driving," in *Proc. Int. Conf. Localization GNSS*, 2016, pp. 1–6.
- [34] K. Haneda et al., "5G 3GPP-like channel models for outdoor urban microcellular and macrocellular environments," in *Proc. IEEE 83rd Veh. Technol. Conf.*, 2016, pp. 1–7.



Yuan Zhang (Graduate Student Member, IEEE) received the B.S. degree in surveying and mapping engineering from the Shandong University of Science and Technology, Qingdao, China, in 2017, and the M.S. degree in geodesy and surveying engineering from Jiangsu Normal University, Xuzhou, China, in 2020. He is currently working toward the Ph.D. degree in information and communication engineering with the College of Electronics and Information Engineering, Tongji University, Shanghai, China.

His research interests include GNSS/5G and multisensor integration for future accurate positioning, optimal sensor placement, and estimation and optimization algorithms.

Mr. Zhang is a Reviewer of several IEEE journals, including IEEE TRANSACTIONS ON INDUSTRIAL INFORMATICS, IEEE TRANSACTIONS ON WIRELESS COMMUNICATIONS, and IEEE SENSORS JOURNAL.



Rui Wang (Senior Member, IEEE) received the Ph.D. degree from the Institute of Wireless Communication Technology (IWCT) at Shanghai Jiao Tong University, Shanghai, China, in 2013.

From 2012 to 2013, he was a Visiting Ph.D. Student with the Department of Electrical Engineering, University of California at Riverside, Riverside, CA, USA. From 2013 to 2014, he was with the Institute of Network Coding, The Chinese University of Hong Kong, as a Postdoctoral Research Associate. From 2014 to 2016, he was an Assistant Professor with the College of Electronics and Information Engineering, Tongji University, Shanghai, where he is currently a Full Professor. He has authored or coauthored more than 60 articles. His research interests include wireless communications, artificial intelligence and wireless positioning.

Dr. Wang was the recipient of the Shanghai Excellent Doctor Degree Dissertation Award in 2015 and ACM Shanghai Rising Star Nomination Award in 2016. He is currently an Associate Editor for IEEE ACCESS and an Editor of the IEEE WIRELESS COMMUNICATIONS LETTERS.



Zhe Xing (Member, IEEE) received the B.S. degree in communication engineering and the M.S. degree in communication and information systems from Sichuan University, Chengdu, China, in 2016 and 2019, respectively, and the Ph.D. degree in information and communication engineering from the College of Electronics and Information Engineering, Tongji University, Shanghai, China, in 2023.

He is currently an Assistant Professor with the School of Information Science and Technology, North China University of Technology, Beijing, China. His research interests include reconfigurable intelligent surface (RIS) and integrated sensing and communication (ISAC).

Dr. Xing was the recipient of the Exemplary Reviewer of the IEEE WIRELESS COMMUNICATIONS LETTERS in 2020. He was a TPC member of the IEEE Global Communications Conference (GLOBECOM) in 2021–2023. He is currently a Reviewer of several IEEE journals, including the IEEE TRANSACTIONS ON COMMUNICATIONS, IEEE TRANSACTIONS ON WIRELESS COMMUNICATIONS, IEEE WIRELESS COMMUNICATIONS LETTERS, and IEEE TRANSACTIONS ON SIGNAL PROCESSING.